# Large eddy simulation of vehicle emissions dispersion process: Implications for on-road remote sensing measurements

Yuhan Huang[a], Elvin C.Y. Ng[a,b], Nic C. Surawski[a], Yat-Shing Yam[c], Wai-Chuen Mok[a,d], Chun-Ho Liu[d], John L. Zhou[a,*], Bruce Organ[a,b], Edward F.C. Chan[a,e]

[a] Centre for Green Technology, School of Civil and Environmental Engineering, University of Technology Sydney, NSW 2007, Australia

[b] Jockey Club Heavy Vehicle Emissions Testing and Research Centre, Vocational Training Council, Hong Kong, China

[c] Environmental Protection Department, Hong Kong Special Administrative Region Government, Hong Kong, China

[d] Department of Mechanical Engineering, The University of Hong Kong, Hong Kong, China

[e] Faculty of Science and Technology, Technological and Higher Education Institute of Hong Kong, Hong Kong, China

Corresponding author:

Prof John L. Zhou, Email: junliang.zhou@uts.edu.au

**Abstract**

On-road remote sensing technology measures concentration ratios of pollutants over $CO_2$ in the exhaust plume in half a second when a vehicle passes by a measurement site, providing a rapid, non-intrusive and economic tool for vehicle emissions monitoring and control. A key assumption in such measurement is that the emission ratios are constant for a given plume. However, there is a lack of study on this assumption, whose validity could be affected by a number of factors, especially the engine operating conditions and turbulence. To guide the development of the next-generation remote sensing system, this study is conducted to investigate the effects of various factors on the emissions dispersion process in the vehicle near-wake region and their effects on remote sensing measurement. The emissions dispersion process is modelled using Large Eddy Simulation (LES). The studied factors include height of the remote sensing system, vehicle speed, acceleration and side wind. The results show that the measurable $CO_2$ and NO exhaust plumes are relatively short at 30 km/h cruising speed, indicating that a large percentage of remote sensing readings with the measurement duration of half a second are below the sensor detection limit which would distort the derived emission ratio. In addition, the valid measurement region of NO/$CO_2$ emission ratio is even shorter than the measurable plume and is at the tailpipe height. The effect of vehicle speed (30-90 km/h) on the measurable plume length is insignificant. Under deceleration condition, the length of the valid NO/$CO_2$ measurement region is shorter than those under cruising and acceleration conditions. Side winds from the far-tailpipe direction have a significant effect on remote sensing measurements. The implications of these findings and possible solutions to improve the accuracy of remote sensing measurement have been proposed and discussed.

***Keywords:*** Computational fluid dynamics; Exhaust plume dispersion; On-road emission test; Near-wake region

**Abbreviations and definitions:**

| | |
|---|---|
| CFD | Computational fluid dynamics |
| DNS | Direct numerical simulation |
| LES | Large eddy simulation |
| LPG | Liquefied petroleum gas |
| PEMS | Portable emission measurement system |
| RANS | Reynolds-Averaged Navier-Stokes |
| RDE | Real driving emissions |
| SGS | Sub-grid scale |
| Emission ratio | Concentration ratio of a pollutant over $CO_2$ (e.g. $NO/CO_2$) |
| Measurable exhaust plume | Concentration larger than 0.1% for $CO_2$ or 10 ppm for NO |
| Valid measurement region of emission ratio | Region with emission ratio close to (within ±10% difference) the original emission ratio in the exhaust pipe |

## 1. Introduction

On-road remote sensing technology is a rapid, non-intrusive and economic tool for use in vehicle emissions monitoring and control under real driving conditions. It measures the concentration ratios of pollutants (e.g. CO, HC and NO) over $CO_2$ in the exhaust plume in half a second when a vehicle passes by a measurement site (Burgard *et al.*, 2006; Cadle and Stephens, 1994; Huang *et al.*, 2018c). These emission ratios are highly useful parameters to evaluate the emissions performance of a vehicle and have been used in various applications worldwide. Since 1 September 2014, the Hong Kong Environmental Protection Department (HKEPD) started using on-road remote sensing technology to detect high-emitting petrol and liquefied petroleum gas (LPG) vehicles for enforcement (HKEPD, 2018). The enforcement program has been very effective in reducing the emissions from petrol and LPG vehicles (Huang *et al.*, 2018b; Organ *et al.*, 2019). However, diesel vehicles, a major source of $NO_x$ emissions, are excluded because the current remote sensing system would likely produce significant false detections of diesel high-emitters. The underlying reasons include low pollutant concentrations and large $CO_2$ variations in the exhaust plume of diesel vehicles due to their non-premixed lean combustion mode. To extend the enforcement program to diesel vehicles, a new generation of remote sensing system with higher accuracy is under development (Huang *et al.*, 2018b).

A key assumption in remote sensing measurement is that the emission ratios are constant for a given plume (Bishop *et al.*, 1989; Burgard *et al.*, 2006). However, there is a lack of study on this assumption, whose validity could be affected by a number of factors such as the engine conditions and vehicle-, exhaust- and wind-induced turbulence. In addition, remote sensing system is placed at a fixed height above the road to measure the emissions of all the passing vehicles, e.g. typically 25 cm for vehicles with bottom arranged tailpipes. However, the tailpipe height varies among vehicle models, as well as vehicle loads. The alignment of the remote sensing light beam to the vehicle tailpipe determines the amount of exhaust gas being measured and thus affects the remote sensing accuracy.

Measuring emissions in the near-wake region of a fast-moving vehicle is challenging. This is because the instantaneous tailpipe emissions in a real driving task are highly dynamic. Remote sensing scans the exhaust plume from tailpipe exit to a few meters downstream in half a second at a frequency of 100 or 200 Hz. In comparison, other emission measurement techniques cannot achieve the required time resolution or measurement region under real driving conditions, and thus are not suitable for investigation of emissions dispersion process for remote sensing applications. Portable emissions measurement system (PEMS) is a standard method to measure real driving emissions (RDE) by carrying measurement instruments on-board the target vehicle (Degraeuwe and Weiss, 2017; Vlachos *et al.*, 2014). However, the time resolution of PEMS is 1 Hz and can only measure the emissions in the tailpipe before dispersion. Plume chasing is a technology that measures the emissions in the wake of a target vehicle by using a following laboratory vehicle carrying measurement instruments (Lau *et al.*, 2015; Ning *et al.*, 2012). However, it can only measure the emissions in the far downstream region (10-15 m) due to safety issues. In addition, the time resolution is only 1-10 seconds and the measurement height (1.5 m) is above the tailpipe. On the other hand, computational fluid dynamics (CFD) modelling is a feasible and economic tool to provide detailed and visualised information about the turbulent flows. It can help the design and development of more accurate remote sensing devices, e.g. for diesel high-emitters enforcement program.

To numerically simulate the turbulence fields, a set of partial differential equations for continuity, momentum (i.e. Navier-Stokes equations), energy and thermodynamic variables need to be solved (Elger *et al.*, 2012). Unfortunately, analytical solutions for the Navier-Stokes equations are not available, except for a few very simple conditions. Therefore, numerical methods are usually used to solve the governing equations. Currently, the most popular numerical approach is the Reynolds-Averaged Navier-Stokes (RANS). In RANS, the local fluctuations and turbulence structures are integrated in the mean quantities. To close the Reynolds stress term, the most widely used models are the $k$-$\varepsilon$ and $k$-$\omega$ two-equation models (Argyropoulos and Markatos, 2015). Chan *et al.* (2001) simulated the initial dispersion process of $NO_x$ from a vehicle exhaust plume using a $k$-$\varepsilon$ turbulence model, and observed that the effect of exhaust-induced turbulence was more dominant than wind-induced turbulence in the vicinity of tailpipe exit. In comparison, wind-induced turbulence gradually became significant for $NO_x$ dispersion with the development of exhaust plume. Amorim *et al.* (2013) evaluated the impact of urban trees on the dispersion of road traffic CO using a standard $k$-$\varepsilon$ turbulence model. The results showed that local air quality was strongly dependent on the synergies between the meteorological conditions, street canyon configuration and trees. Bhautmage and Gokhale (2016) investigated the effects of moving-vehicle wakes on pollutant dispersion in a highway road tunnel by realizable $k$-$\varepsilon$ model. Woo *et al.* (2016) investigated the influence of a leading vehicle's exhaust plume on a following mobile laboratory vehicle's air quality measurements using both PEMS experiments and CFD simulation (standard $k$-$\varepsilon$ model).

However, the modelling ability of RANS is only limited to the large flow structures. With the fast increase of computational power, more advanced turbulence models are becoming feasible in recent years, such as Large Eddy Simulation (LES) and Direct Numerical Simulation (DNS). DNS solves all the turbulence fluctuations and structures without averaging or using turbulence models, providing the most accurate numerical solution to turbulence flows. However, DNS is only applicable to fundamental research applications with low Reynolds numbers, and thus is not applicable to most practical applications due to its tremendous requirement for computer speed and memory (Argyropoulos and Markatos, 2015; Elger *et al.*, 2012). LES is a compromise between RANS and DNS (Spalart, 2000), in which the larger-scale flow structures are explicitly computed while the effect of sub-grid scale (SGS) motions is modelled (Veynante and Vervisch, 2002). LES offers the ability to see more detailed flow structures (Spalart, 2000). In view of the limited computational resource, LES is more applicable for flow fields with a moderate Reynolds number and geometry size (Rutland, 2011). Several studies have utilised LES to simulate the emissions dispersion process. Dong and Chan (2006) and Chan *et al.* (2008) used LES to simulate the dispersion of $NO_x$ and CO in the near-wake region of a light-duty diesel vehicle. Gallagher *et al.* used LES to investigate the effect of various factors on the dispersion of gaseous emissions from the street to footpath region in a street canyon, including passive control system (e.g. parked cars, low boundary walls) (Gallagher *et al.*, 2011, 2013), wind conditions and fleet composition (Gallagher, 2016), and geometrical details of parked cars and mesh size (Gallagher and Lago, 2019). Aristodemou *et al.* (2018) used an LES model to investigate the effect of tall buildings on air flows and pollutants dispersion.

As reviewed, on-road remote sensing is considered an effective and economic tool to monitor emissions of vehicle fleets in the real world. However, there is a lack of investigation on the fundamental assumption of its measurement principle, and a thorough understanding of the tailpipe emissions dispersion process is of great importance for the development of the next-generation remote sensing system for diesel high-emitters enforcement. Therefore, this study is conducted to unprecedentedly investigate the effect of various factors on emissions dispersion process in the vehicle near-wake region using LES, with a special focus on its effect on emissions measurement using on-road remote sensing technology. The implications of the CFD results and possible solutions to improve the accuracy of remote sensing measurement are discussed.

## 2. Numerical models

### 2.1. *Computational mesh*

**Fig. S1** (Supplementary Material) shows the computational domain (a), dimensions of the vehicle body (b) and computational mesh (c). As shown in **Fig. S1(a)**, the computational domain is a rectangular box of 20 m × 6 m × 5 m. The studied vehicle is a diesel-fuelled Toyota HiAce with an engine displacement of 2982 cc (**Fig. S1(b)**), which is placed at 4 m in the computational domain. Toyota HiAce is the most popular diesel vehicle model in Hong Kong, accounting for 19% of total remote sensing records (Huang *et al.*, 2018a). The computational mesh is generated using the *ANSYS Meshing*. As shown in **Fig. S1(c)**, the computational mesh mainly consists of tetrahedral grids. It is generated according to the best practice guideline for flows in the urban environment (Franke *et al.*, 2007; Gallagher *et al.*, 2011). The general grid size is 0.10 m. However, the grids in the near-wake region of the vehicle (the area of the main interest) are refined to 0.05 m. The grids around the vehicle surface, exhaust pipe and ground are also refined to capture the flow characteristics around the boundary layer and exhaust pipe. The total number of nodes is 1384083.

### 2.2. *Computational model*

The numerical model is developed using the CFD code *ANSYS Fluent 19.2* (ANSYS, 2019). In this study, the Reynolds numbers ($Re = \rho u L/\mu$) are in the ranges of $2.5\times10^5$ – $3.2\times10^6$ and $1.5\times10^4$ – $4.8\times10^4$ for air and exhaust gas flows, respectively. The ambient air and exhaust gas flows are simulated using the LES approach. The SGS flows are simulated using the Wall-Adapting Local Eddy-Viscosity (WALE) model which provided several advantages over the classical Smagorinsky formulation, including the detection of all turbulence structures relevant for kinetic energy dissipation, correct wall asymptotic behaviour for wall bounded flows, and correct treatment of laminar zones in the domain (Nicoud and Ducros, 1999). Mass, energy and momentum conservation, heat transfer, and species transfer equations are numerically solved. Diesel vehicles are relatively clean in CO and HC emissions (Huang *et al.*, 2019a; Huang *et al.*, 2019b) but are the major sources of NO pollution in cities (Anenberg *et al.*, 2017). Therefore, five gas species including $N_2$, $O_2$, $H_2O$, $CO_2$ and NO are considered. NO is considered an inert species in this study because remote sensing only measures the exhaust emissions from the tailpipe exit to a few meters downstream in half a second which is relatively short compared with the time scales of $NO_x$-$O_3$ reactions (tens of seconds) (Vardoulakis *et al.*, 2003). The pressure-velocity coupling scheme is the Semi-Implicit Method for Pressure Linked Equations (SIMPLE) method. The spatial discretization methods are Least Squares Cell Based for gradient, Second Order for pressure, Bounded Central Differencing for momentum and Second Order Upwind for energy and species transport. Transient simulations are carried out with a time step increment of 0.01 s. The convergence criteria are residual values of $10^{-3}$ for continuity, velocity and species, and $10^{-6}$ for energy. The maximum number of iterations is 30 per time step. 1000 steps are performed to obtain reliable and developed exhaust plumes. **Fig. S2** shows the temporal variation of $CO_2$ concentrations at different distances downstream the tailpipe exit. It shows that the $CO_2$ concentration becomes relatively stable after 200 steps, although with slight variations. Therefore, the instantaneous images shown are representative of the pollutant dispersion in the near-wake region of a vehicle. In Section 3, the plume lengths are the averaged values between time steps 250 and 1000.

### *2.3. Boundary and initial conditions*

In this study, various vehicle speed, acceleration and wind conditions are simulated because they are the primary parameters determining the exhaust plume conditions and the flow fields in the vehicle near-wake region, which affect the emissions dispersion process and consequently the remote sensing measurement. **Table S1** (Supplementary Material) presents the boundary and initial conditions used in the simulation. In all the simulated cases, the ambient air temperature is 300 K and standard air compositions are used. Vehicle speed and acceleration are the key parameters that determine the engine operation conditions and thus the tailpipe emissions, which are also the key parameters that affect the flow fields around the vehicle (vehicle and exhaust induced turbulence). In this study, four vehicle speeds (7, 30, 60 and 90 km/h) and three accelerations (-3, 0, +3 km/h/s) are simulated. 7 km/h is the lowest speed that can be measured in remote sensing and 90 km/h is the highest speed tested in the Hong Kong Transient Emission Test (HKTET), which is the test cycle for ascertaining the rectification of the excessive emission problem of in-use vehicles with the aid of a chassis dynamometer. Therefore, 7-90 km/h is the range of driving conditions that is used in remote sensing analysis. Side wind is another key parameter that affects the flow field around the vehicle (wind induced turbulence). In this study, seven side wind speed conditions are simulated, namely 0, ±2, ±6 and ±12 m/s which correspond to calm (Beaufort scale 0), light breeze (Beaufort scale 2), moderate breeze (Beaufort scale 4) and strong breeze (Beaufort scale 6), respectively.

To obtain boundary conditions at the tailpipe exit, a RDE test on a Toyota HiAce was conducted using PEMS. During the RDE test, the vehicle speed, exhaust flow rate, exhaust gas concentrations and exhaust temperature were measured at a frequency of 1 Hz. More details about the PEMS equipment can be found in Huang *et al.* (2019c). **Fig. S3** shows the driving speed, $CO_2$ concentration and exhaust temperature profiles of the RDE test. As shown in **Fig. S3**, a RDE test is highly dynamic. Therefore, the average values of exhaust flow rate, temperature and concentrations were calculated from the RDE data under each simulated vehicle speed and acceleration condition. The exhaust gas speed at the tailpipe exit is calculated from the tailpipe diameter of 63.5 mm (2.5 inches) and the PEMS data of exhaust flow rate and temperature. A high-emitting event of $NO/CO_2$ = 50 ppm/% is simulated for all cases.

*2.4. Mesh independence and model verification*

Mesh quality is an important concern in CFD modelling. To achieve mesh independence, three meshes with different grid sizes have been tested, namely Mesh 1 (816900 nodes), Mesh 2 (1384083 nodes) and Mesh 3 (1840211 nodes). **Fig. 1** compares the averaged $CO_2$ concentration along the tailpipe centreline as a result of different mesh densities. Compared with Mesh 2 (medium mesh), Mesh 1 (coarse mesh) over-predicts $CO_2$ concentration within 0.15 m but under-predicts it in the further downstream. When the mesh is refined from Mesh 2 to Mesh 3 (fine mesh), the two profiles become almost identical within 0.2 m, but Mesh 3 slightly over-predicts it between 0.2 and 3.0 m. In general, the difference between the two calculated profiles becomes relatively small, indicating that mesh independence is achieved. The computation time using Mesh 2 is about 40 hours per run using 24 cores of a 2.3 GHz Intel Xeon E5-2695 v3 workstation, while the computation time of Mesh 3 is 70% longer than that of Mesh 2. Therefore, Mesh 2 is considered sufficient to perform the simulations with a reasonable accuracy and low computational cost.

To verify the CFD model, a diesel Toyota HiAce vehicle was tested under idling condition to obtain the $CO_2$ concentration and gas temperature distributions downstream the tailpipe. $CO_2$ concentration was measured by an EMS 5003 gas analyser and gas temperature was measured by a K-type thermocouple. As shown in **Fig. 2**, the model well predicts $CO_2$ concentrations and exhaust temperature within 0.3 m and after 3.0 m, but over-predicts them between 0.3 and 3.0 m. Although $CO_2$ is over-predicted at some region, it will not under-estimate the $NO/CO_2$ ratio because the emissions dispersion process is in essence the mixing of exhaust plume, which carries the emissions, with the ambient air, so that $CO_2$, NO and temperature show the same distribution pattern in the region close to the tailpipe exit (**Fig. S4**). This indicates that NO will also be over-predicted to the same extent as $CO_2$ and temperature (**Fig. 2**), thus $NO/CO_2$ ratio will not be under-predicted. This also justifies the validation method using temperature and $CO_2$ which can be easily and reliably measured. The over-prediction of $CO_2$ and temperature would be caused by the simplification of the vehicle geometry, in which the tailpipe is horizontal while it is slightly bent towards the ground in a real HiAce. The over-prediction in the medium distance downstream was also reported by Chan *et al.* (2001). In the real world, some rear-arranged tailpipes are with a slight bent exit, which would lead to shorter measurable exhaust plumes at the tailpipe height than horizontal tailpipes, if the other conditions (mainly exhaust flow rate and gas concentrations) are the same. A shorter plume will be more challenging for remote sensing measurement as remote sensing sensors are placed at a fixed height above road surface, which will be further discussed in **Fig. 4**. Overall, the fast dispersion of the experimental exhaust plume, as a key phenomenon, has been well captured by the LES model.

## 3. Results and discussion

The CFD results are presented and discussed as follows. Section 3.1 reports exhaust plume dispersion process at vehicle speed of 30 km/h, acceleration of 0 km/h/s and side wind of 0 m/s. The distributions of air velocity, dynamic pressure, temperature, emission concentrations and emission ratios are visualised, and the effects of emissions dispersion and tailpipe height on remote sensing measurement are analysed. Sections 3.2, 3.3 and 3.4 investigate the effects of vehicle speed, acceleration and side wind on emissions dispersion process and remote sensing measurement, respectively. 30 km/h is used as the base vehicle speed because it is the typical speed when vehicles pass by a remote sensing site (**Fig. S5**).

### *3.1. Emissions dispersion process*

**Fig. 3** shows the velocity (a), dynamic pressure (b) and temperature (c) fields around the vehicle on the vertical and horizontal cut-planes that pass through the tailpipe centreline. The results demonstrate that the air flow speed is slow in the vehicle near-wake region (**Fig. 3(a)**), leading to a low dynamic pressure ($q = ½ \rho u^2$) region (**Fig. 3(b)**). The exhaust temperature reduces quickly to ambient temperature in a very short distance after the tailpipe exit (**Fig. 3(c)**). In general, the effect of the exhaust gas flow on the overall air flow fields of velocity, dynamic pressure and temperature is insignificant due to its small mass.

**Fig. 4** visualises the distribution of the absolute volume concentrations of $CO_2$ (a) and NO (b) emissions in the vehicle near-wake region. Areas with concentrations lower than 0.1% for $CO_2$ and 10 ppm for NO are clipped to demonstrate the exhaust plume length, which are about the typical detection limits of $CO_2$ and NO in PEMS, respectively (Horiba, 2017), while the detection limits of remote sensing system are much higher than PEMS (Huang *et al.*, 2018b). Therefore, the measurable exhaust plume is defined as the main plume (excluding the detached discrete plume areas) with emission concentration larger than 0.1% for $CO_2$ or 10 ppm for NO. Using this definition, **Fig. 4** shows that the $CO_2$ plume lengths are 2.7 ± 1.1 m in the top vertical plane and 1.5 ± 0.2 m in the bottom horizontal plane, and the NO plume lengths are 1.4 ± 0.2 and 1.1 ± 0.3 m, respectively. In comparison, NO plume is smaller than $CO_2$ plume due to its much lower concentration (at ppm level) than that of $CO_2$ (at % level) in the engine exhaust gas.

However, a remote sensing measurement lasts for half a second at 200 Hz when a vehicle passes by the measurement site, which is equivalent to 4.2 m at the studied vehicle speed of 30 km/h. **Fig. 4** indicates that at least 36%-74% of the remote sensing measurements are meaningless for a given plume, because the $CO_2$ and NO concentrations are below the sensitivity of a remote sensor after 1.1-2.7 m. For each exhaust plume, remote sensing records

100 readings of NO and $CO_2$ emission concentrations, and plots NO against $CO_2$ to derive the least square slope, i.e. NO/$CO_2$ ratio. The large percentage of meaningless data points (around the origin, as shown in Fig. 2 of Bishop *et al.* (1989)) would distort the derived emission ratio, and thus reduce the accuracy of remote sensing. This suggests that using a shorter measuring duration and a higher remote sensing frequency could improve the accuracy.

As an indirect measurement technique, remote sensing can only determine the concentration ratio of NO/$CO_2$ rather than the absolute concentration of NO or $CO_2$, and a key assumption is that NO/$CO_2$ ratio is constant for a given plume. **Fig. 5** shows the distribution of NO/$CO_2$ ratio in the vertical (top) and horizontal (bottom) cut-planes passing through the tailpipe centreline. In this study, the NO/$CO_2$ value is 50 ppm/% at the tailpipe exit. However, as shown in **Fig. 5**, the assumption that NO/$CO_2$ ratio is constant is only valid within a very short distance due to the different dispersion rates of NO and $CO_2$ in the further downstream region. This is because the exhaust gas speed is high in the region close to the tailpipe exit, so that the mixing and dispersion are mainly controlled by the high momentum of the exhaust gas. As a result, NO and $CO_2$ disperse at the same rate, leading to the unchanged NO/$CO_2$ ratio near the tailpipe exit. This is proven by the results shown in **Fig. S4** that $CO_2$ and NO emissions demonstrate the same distribution as the exhaust temperature in the region near the tailpipe exit (within ~ 1 m). However, in the further downstream region, the exhaust gas speed and momentum reduce quickly, so that the molecular diffusion process becomes the dominant factor. At ambient temperature of 300 K, the diffusion coefficients in air are 15.84 $mm^2/s$ for $CO_2$ and 23.69 $mm^2/s$ for NO, respectively (Yaws, 2003, 2010). Therefore, NO disperses more quickly than $CO_2$ does, leading to the reduced NO/$CO_2$ ratio in the further downstream region.

NO/$CO_2$ ratio is 50 ppm/% at the tailpipe exit but then reduces gradually with the development of the exhaust plume. To quantify the analysis, the valid measurement region of emission ratio is defined as regions with emission ratio close to (within ±10% difference) that of the original emission ratio in the exhaust pipe, i.e. 45-50 ppm/% in this study. Using this definition, the lengths of the valid measurement region for remote sensing are only about 1.2 ± 0.4 m in the vertical plane and 1.1 ± 0.3 m in the horizontal plane. The valid measurement region of emission ratio is even shorter than that of measurable exhaust plume. This further indicates that the currently used remote sensing measurement duration of half a second for one passing vehicle is too long and would cause additional uncertainties.

In addition, remote sensing systems are placed at a fixed height to measure emissions of all the passing vehicles. However, tailpipe height varies among vehicle models, as well as vehicle loads. **Fig. 5** shows that the valid measurement region of $NO/CO_2$ ratio is only at the tailpipe height. Remote sensing system would measure no emissions if the sensor is lower than the tailpipe, and would measure much lower $NO/CO_2$ ratios if the sensor is higher than the tailpipe. To more accurately measure the emissions from different vehicles, one possible solution is using multiple remote sensors with different vertical heights in one remote sensing system, and only use data from the sensor that has the strongest signals, which is more likely aligned with the tailpipe centreline. Another promising method is a facing-down remote sensing configuration which is currently under development.

### *3.2. Effect of vehicle speed*

**Fig. 6(a)** shows the effect of vehicle speed on the measurable $CO_2$ plume length (> 0.1% concentration) on the vertical cut-plane crossing the tailpipe centreline, including 7, 30, 60 and 90 km/h. **Table S2** provides the lengths of the measurable $CO_2$ and $NO/CO_2$ plumes as a function of the vehicle speed. As shown in **Fig. 6(a)**, at 7 km/h vehicle speed, the turbulence included by the vehicle is weak and does not significantly affect the exhaust plume. As a result, the exhaust plume is slim and long, with a measurable $CO_2$ plume length of 3.9 ± 1.9 m. The plume is generally distributed horizontally at the tailpipe height. Higher vehicle speed induces stronger turbulence and thus enhances the mixing and dispersion processes of exhaust emissions. In addition, higher vehicle speed induces some vortices in the near wake region, which entrain some exhaust gas into the near-wake region above the tailpipe. Consequently, the measurable $CO_2$ plume lengths of 30-90 km/h vehicle speeds are significantly shorter than that of 7 km/h, but they remain relatively constant from 30 to 90 km/h (with 2.7 ± 1.1 m @ 30 km/h, 2.1 ± 0.4 m @ 60 km/h and 2.1 ± 0.2 m @ 90 km/h).

Regarding the length of the valid measurement region of $NO/CO_2$ ratio (i.e. 45-50 ppm/%), **Fig. 6(b)** shows that it generally reduces with increasing vehicle speed, with 1.9 ± 0.4 m at 7 km/h, 1.2 ± 0.4 m at 30 km/h, 0.7 ± 0.1 m at 60 km/h and 1.0 ± 0.4 m at 90 km/h. It is worth noting that the measurable plume lengths (2.1-3.9 m, **Fig. 6(a)**) are always longer than the valid measurement region of $NO/CO_2$ (0.7-1.9 m, **Fig. 6(b)**). However, both lengths are critical for remote sensing: the measurable plume length determines the region in which meaningful remote sensing readings can be made, while the valid measurement length determines the region in which remote sensing readings can be used to derive the correct $NO/CO_2$ ratio. The shorter one limits the plume length that can be used for remote sensing measurement.

In a real-world remote sensing program, 7 km/h is the lower measurement limit of vehicle speed and most vehicles are driven faster than 7 km/h. Higher vehicle speed induces stronger turbulence which enhances exhaust plume dispersion. On the other hand, higher vehicle speed requires bigger engine load and thus produces higher exhaust flow rate which prolongs the exhaust dispersion. Therefore, the effect of vehicle speed (30-90 km/h) on the lengths of measurable $CO_2$ plume and valid $NO/CO_2$ measurement region is not obvious. This finding suggests that vehicle speed would not significantly affect the remote sensing measurement. High vehicle speed like 90 km/h would even be better for a reliable remote sensing measurement as the engine produces sufficient exhaust gas.

### 3.3. *Effect of acceleration*

**Fig. 7(a)** shows the effect of vehicle acceleration on the measurable $CO_2$ plume length (> 0.1% concentration), including moderate deceleration of -3 km/h/s, cruising (0 km/h/s) and moderate acceleration of +3 km/h/s. PEMS data show that under the same vehicle speed condition (i.e. 30 km/h), there are insignificant differences in the exhaust temperature and $CO_2$ concentration between deceleration (534 K and 6.1%), cruising (548 K and 9.0%) and acceleration (567 K and 9.1%) for the studied HiAce diesel vehicle. The major differences are in the exhaust flow rates, with 32.8, 49.3 and 135.0 L/s for deceleration, cruising and acceleration, respectively, due to higher fuel consumption and engine speed at higher load. Therefore, as shown in **Fig. 7(a)**, the measurable $CO_2$ plume length under deceleration condition (1.6 ± 0.5 m) is shorter than that under cursing (2.7 ± 1.1 m) or acceleration (4.6 ± 1.9 m) condition. Such a short plume would be too challenging to be measured by remote sensing and the derived least square slope (i.e. $NO/CO_2$) would include high uncertainties. Regarding the valid measurement region of emission ratio for remote sensing, **Fig. 7(b)** shows that the valid measurement region with $NO/CO_2$ ratio between 45 and 50 is relatively short under deceleration condition (0.7 ± 0.1 m) compared with acceleration (2.3 ± 0.5 m). These results suggest that remote sensing measurements under deceleration conditions would have larger uncertainties and should be used with caution. Fuel injection would be even stopped (thus no exhaust emissions) under strong deceleration conditions, e.g. typically < -5 kW/t vehicle specific power (VSP) for passenger cars (Bernard *et al.*, 2018). Therefore, it is recommended to use remote sensing measurements under steady speed or moderate acceleration conditions which generate sufficient amount of exhaust plumes for accurate measurements.

### *3.4. Effect of side wind*

**Fig. 8** shows the effect of side wind on the $CO_2$ plume and $NO/CO_2$ ratio on a horizontal cut-plane passing through the tailpipe centreline, including calm (0 m/s), light breeze (±2 m/s, Beaufort scale 2), moderate breeze (±6 m/s, Beaufort scale 4) and strong breeze (±12 m/s, Beaufort scale 6). Side winds from different directions are simulated, where "+" indicates that the side wind comes from the tailpipe side of the vehicle while "-" indicates that the side wind comes from opposite side. The arrows in **Fig. 8** indicate the relative air velocity vectors to the vehicle. As shown in **Fig. 8**, when side wind speed increases from 0 to +12 m/s, $CO_2$ plume bends with the side wind and the measurable $CO_2$ plume length does not change significantly. However, when side wind speed increases from 0 to -12 m/s, the measurable $CO_2$ plume becomes very short even under light breeze condition of -2 m/s. This is mainly because when the side wind comes from the far-tailpipe side, the relative air velocity vector has an angle with the vehicle body. As a result, the vehicle body blocks the wind and generates vortices (i.e. stronger turbulence) in the near-wake and leeward region. These vortices entrain the exhaust plume to the upper right region in the vehicle near wake region, leading to the greatly reduced plume lengths observed in **Fig. 8**. Regarding the valid measurement region of $NO/CO_2$ ratio (45-50 ppm/%), **Fig. 8** shows that it reduces significantly with the increase of far-tailpipe side winds, but not obviously for tailpipe side winds. These results suggest that side winds from the far-tailpipe direction would have a significant effect on remote sensing measurement in terms of measurable $CO_2$ plume and valid $NO/CO_2$ region, and thus remote sensing measurements should ideally be taken under calm conditions.

## 4. Conclusions

In this study, LES modelling was performed to assess the effects of various factors on emissions dispersion process in the vehicle near-wake region and their effects on emissions measurement using on-road remote sensing technology. The simulated factors included remote sensing height, vehicle speed, acceleration and side wind. The major results are summarised as follows:

1) The lengths of measurable $CO_2$ and NO plumes and valid $NO/CO_2$ measurement region are relatively short at 30 km/h cruising speed, suggesting that the currently used measurement duration of half a second would be too long. Using a higher remote sensing frequency and a shorter measurement duration should improve the accuracy. In addition, the valid $NO/CO_2$ measurement region is at the tailpipe height, so that measurement would be inaccurate if the remote sensing beam is not well aligned with the tailpipe. A downward-facing configuration or an array of beams with different heights could help improve remote sensing accuracy.

2) The exhaust plume is slim and long at 7 km/h vehicle speed, but becomes significantly shorter at higher vehicle speeds. The effect of vehicle speed (30-90 km/h) on the lengths of measurable $CO_2$ plume and valid $NO/CO_2$ measurement region is insignificant, due to the competing effects of stronger vehicle induced turbulence and higher exhaust flow rate.

3) Under deceleration condition (-3 km/h/s), the measurable $CO_2$ plume and the valid $NO/CO_2$ measurement region are shorter than those under cruising (0 km/h/s) and acceleration (+3 km/h/s) conditions due to lower exhaust flow rate. This suggests that remote sensing measurements should be taken under steady speed or moderate acceleration conditions which generate sufficient amount of exhaust plumes for accurate measurements.

4) Far-tailpipe side winds reduce the lengths of the measurable plume and valid $NO/CO_2$ measurement region, especially for those from the far-tailpipe side. Therefore, remote sensing should ideally be used under calm conditions.

## Acknowledgement

The authors would like to express their great appreciation to Mr. Leo C.H. Chan at the Jockey Club Heavy Vehicle Emissions Testing and Research Centre for the technical assistance and support in the idling emission tests.

## References

J.H. Amorim, V. Rodrigues, R. Tavares, *et al.*, 2013. CFD modelling of the aerodynamic effect of trees on urban air pollution dispersion. *Sci. Total Environ.* 461-462, 541-551.

S.C. Anenberg, J. Miller, R. Minjares, *et al.*, 2017. Impacts and mitigation of excess diesel-related NOx emissions in 11 major vehicle markets. *Nature* 545, 467-471.

ANSYS, 2019. ANSYS 19.2 — Next-Generation Pervasive Engineering Simulation. https://www.leapaust.com.au/ansys-release-19/ <accessed 05.12.2019>.

C.D. Argyropoulos, N.C. Markatos, 2015. Recent advances on the numerical modelling of turbulent flows. *Appl. Math. Model.* 39, 693-732.

E. Aristodemou, L.M. Boganegra, L. Mottet, *et al.*, 2018. How tall buildings affect turbulent air flows and dispersion of pollution within a neighbourhood. *Environ. Pollut.* 233, 782-796.

Y. Bernard, U. Tietge, J. German, *et al.*, 2018. Determination of real-world emissions from passenger vehicles using remote sensing data. *The Real Urban Emissions (TRUE) Initiative*.

U. Bhautmage, S. Gokhale, 2016. Effects of moving-vehicle wakes on pollutant dispersion inside a highway road tunnel. *Environ. Pollut.* 218, 783-793.

G.A. Bishop, J.R. Starkey, A. Ihlenfeldt, *et al.*, 1989. IR Long-Path Photometry: A Remote Sensing Tool for Automobile Emissions. *Anal. Chem.* 61, 671A-677A.

D.A. Burgard, G.A. Bishop, R.S. Stadtmuller, *et al.*, 2006. Spectroscopy Applied to On-Road Mobile Source Emissions. *Appl. Spectrosc.* 60, 135A-148A.

S.H. Cadle, R.D. Stephens, 1994. Remote sensing of vehicle exhaust emission. *Environ. Sci. Technol.* 28, 258A-264A.

T.L. Chan, G. Dong, C.S. Cheung, *et al.*, 2001. Monte Carlo simulation of nitrogen oxides dispersion from a vehicular exhaust plume and its sensitivity studies. *Atmos. Environ.* 35, 6117-6127.

T.L. Chan, D.D. Luo, C.S. Cheung, *et al.*, 2008. Large eddy simulation of flow structures and pollutant dispersion in the near-wake region of the studied ground vehicle for different driving conditions. *Atmos. Environ.* 42, 5317-5339.

B. Degraeuwe, M. Weiss, 2017. Does the New European Driving Cycle (NEDC) really fail to capture the NOx emissions of diesel cars in Europe? *Environ. Pollut.* 222, 234-241.

G. Dong, T.L. Chan, 2006. Large eddy simulation of flow structures and pollutant dispersion in the near-wake region of a light-duty diesel vehicle. *Atmos. Environ.* 40, 1104-1116.

D.F. Elger, B.C. Williams, C.T. Crowe, *et al.*, 2012. Engineering Fluid Mechanics (10th Edition). Wiley.

J. Franke, A. Hellsten, H. Schlünzen, *et al.*, 2007. Best Practice Guideline for the CFD Simulation of Flows in the Urban Environment. *University of Hamburg*.

J. Gallagher, 2016. A modelling exercise to examine variations of NOx concentrations on adjacent footpaths in a street canyon: The importance of accounting for wind conditions and fleet composition. *Sci. Total Environ.* 550, 1065-1074.

J. Gallagher, L.W. Gill, A. McNabola, 2011. Optimizing the use of on-street car parking system as a passive control of air pollution exposure in street canyons by large eddy simulation. *Atmos. Environ.* 45, 1684-1694.

J. Gallagher, L.W. Gill, A. McNabola, 2013. The passive control of air pollution exposure in Dublin, Ireland: A combined measurement and modelling case study. *Sci. Total Environ.* 458-460, 331-343.

J. Gallagher, C. Lago, 2019. How parked cars affect pollutant dispersion at street level in an urban street canyon? A CFD modelling exercise assessing geometrical detailing and pollutant decay rates. *Sci. Total Environ.* 651, 2410-2418.

HKEPD, 2018. Strengthened Emissions Control for Petrol and LPG Vehicles. http://www.epd.gov.hk/epd/english/environmentinhk/air/guide_ref/remote_sensing_Petrol_n_LPG.htm <accessed 25.09.2019>.

Horiba, 2017. Specifications of Horiba On-Board Emissions Measurement System OBS-2200.

Y. Huang, E.C.Y. Ng, Y.-s. Yam*, et al.*, 2019a. Impact of potential engine malfunctions on fuel consumption and gaseous emissions of a Euro VI diesel truck. *Energy Convers. Manage.* 184, 521-529.

Y. Huang, B. Organ, J.L. Zhou*, et al.*, 2018a. Emission measurement of diesel vehicles in Hong Kong through on-road remote sensing: Performance review and identification of high-emitters. *Environ. Pollut.* 237, 133-142.

Y. Huang, B. Organ, J.L. Zhou*, et al.*, 2018b. Remote sensing of on-road vehicle emissions: Mechanism, applications and a case study from Hong Kong. *Atmos. Environ.* 182, 58-74.

Y. Huang, B. Organ, J.L. Zhou*, et al.*, 2019b. Characterisation of diesel vehicle emissions and determination of remote sensing cutpoints for diesel high-emitters. *Environ. Pollut.* 252, 31-38.

Y. Huang, N.C. Surawski, B. Organ*, et al.*, 2019c. Fuel consumption and emissions performance under real driving: Comparison between hybrid and conventional vehicles. *Sci. Total Environ.* 659, 275-282.

Y. Huang, Y.S. Yam, C.K.C. Lee*, et al.*, 2018c. Tackling nitric oxide emissions from dominant diesel vehicle models using on-road remote sensing technology. *Environ. Pollut.* 243, 1177-1185.

C.F. Lau, A. Rakowska, T. Townsend*, et al.*, 2015. Evaluation of diesel fleet emissions and control policies from plume chasing measurements of on-road vehicles. *Atmos. Environ.* 122, 171-182.

F. Nicoud, F. Ducros, 1999. Subgrid-Scale Stress Modelling Based on the Square of the Velocity Gradient Tensor. *Flow Turbul. Combust.* 62, 183-200.

Z. Ning, M. Wubulihairen, F. Yang, 2012. PM, NOx and butane emissions from on-road vehicle fleets in Hong Kong and their implications on emission control policy. *Atmos. Environ.* 61, 265-274.

B. Organ, Y. Huang, J.L. Zhou*, et al.*, 2019. A remote sensing emissions monitoring programme reduces emissions of gasoline and LPG vehicles. *Environ. Res.* 177, 108614.

C.J. Rutland, 2011. Large-eddy simulations for internal combustion engines – a review. *Int. J. Engine Res.* 12, 421-451.

P.R. Spalart, 2000. Strategies for turbulence modelling and simulations. *Int. J. Heat Fluid Flow* 21, 252-263.

S. Vardoulakis, B.E.A. Fisher, K. Pericleous*, et al.*, 2003. Modelling air quality in street canyons: a review. *Atmos. Environ.* 37, 155-182.

D. Veynante, L. Vervisch, 2002. Turbulent combustion modeling. *Prog. Energy Combust. Sci.* 28, 193-266.

T.G. Vlachos, P. Bonnel, A. Perujo*, et al.*, 2014. In-Use Emissions Testing with Portable Emissions Measurement Systems (PEMS) in the Current and Future European Vehicle Emissions Legislation: Overview, Underlying Principles and Expected Benefits. *SAE Int. J. Commer. Veh.* 7, 199-215.

S.-H. Woo, K.-H. Kwak, G.-N. Bae*, et al.*, 2016. Overestimation of on-road air quality surveying data measured with a mobile laboratory caused by exhaust plumes of a vehicle ahead in dense traffic areas. *Environ. Pollut.* 218, 1116-1127.

C.L. Yaws, 2003. Yaws' Handbook of Thermodynamic and Physical Properties of Chemical Compounds. Knovel.

C.L. Yaws, 2010. Yaws' Transport Properties of Chemicals and Hydrocarbons (Electronic Edition). Knovel.

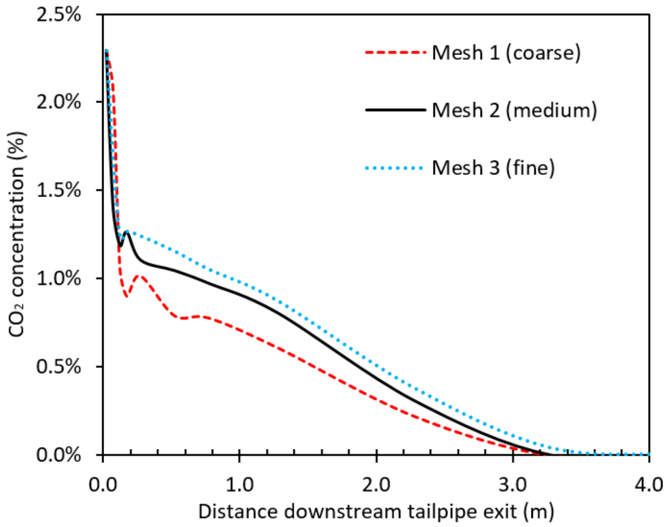


**Fig. 1**. Mesh independence test.

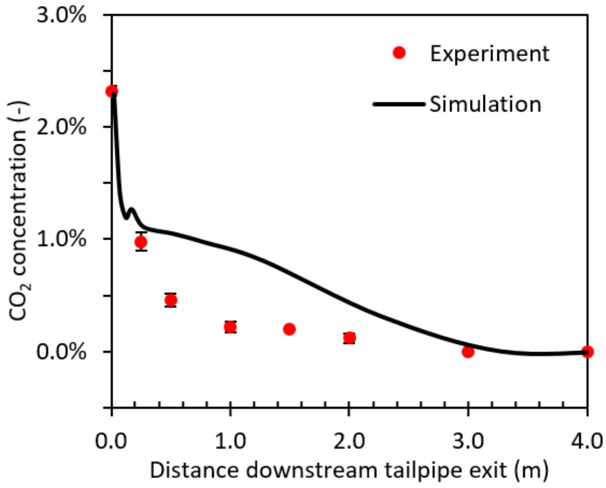


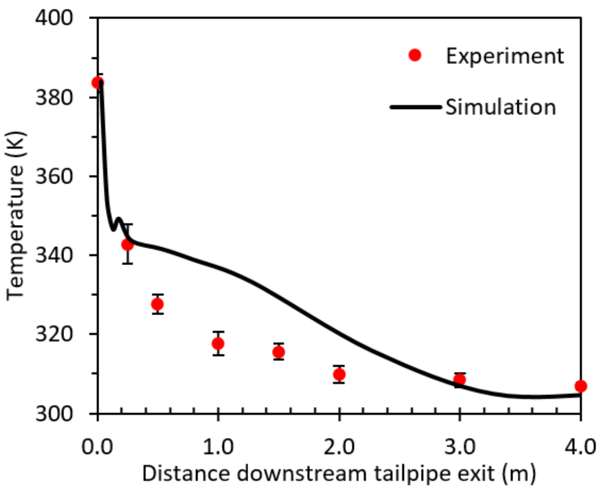


**Fig. 2**. Comparison of simulated and measured $CO_2$ concentrations and gas temperatures.

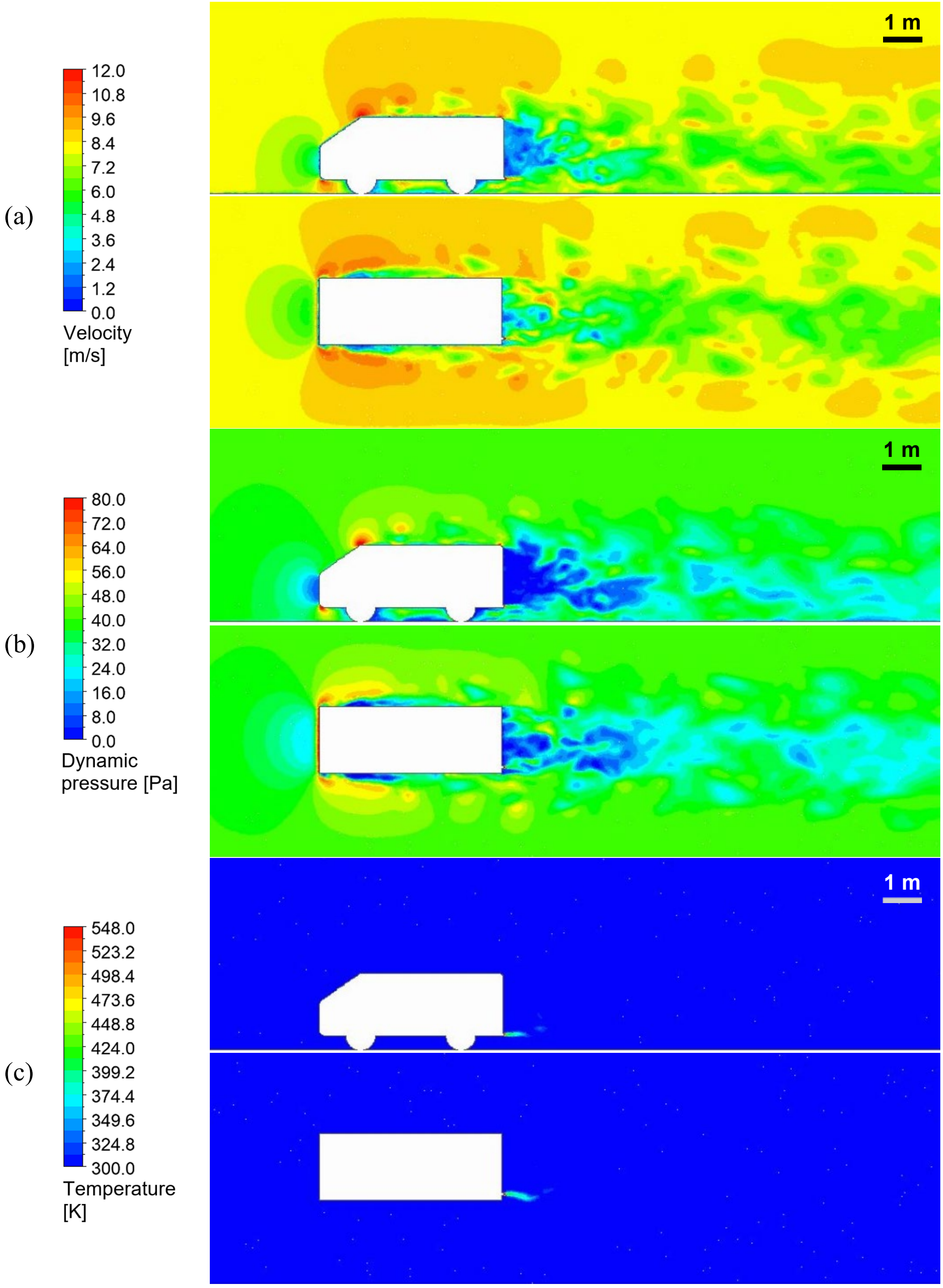


552 **Fig. 3.** Velocity (a), dynamic pressure (b) and temperature (c) around the vehicle under

553 vehicle speed of 30 km/h, acceleration of 0 km/h/s and side wind of 0 m/s.

554

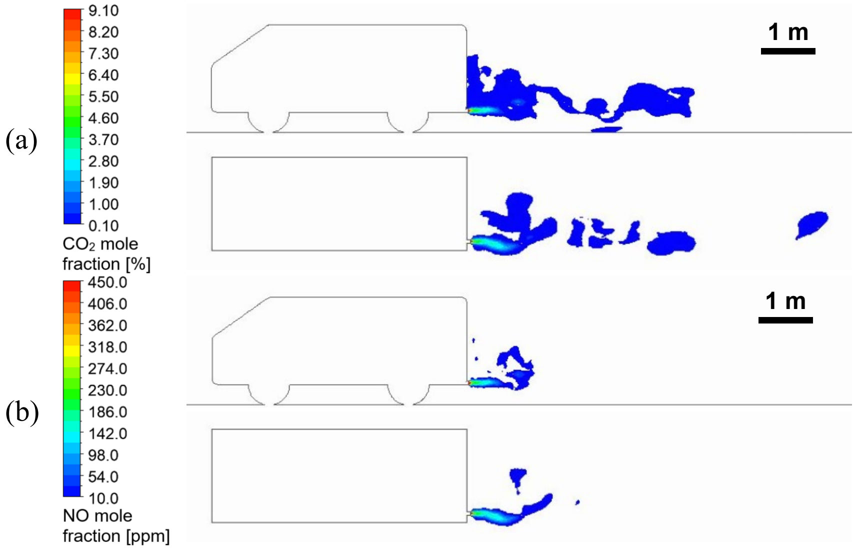


**Fig. 4.** Absolute volume concentrations of $CO_2$ (a) and NO (b) under vehicle speed of 30 km/h, acceleration of 0 km/h/s and side wind of 0 m/s.

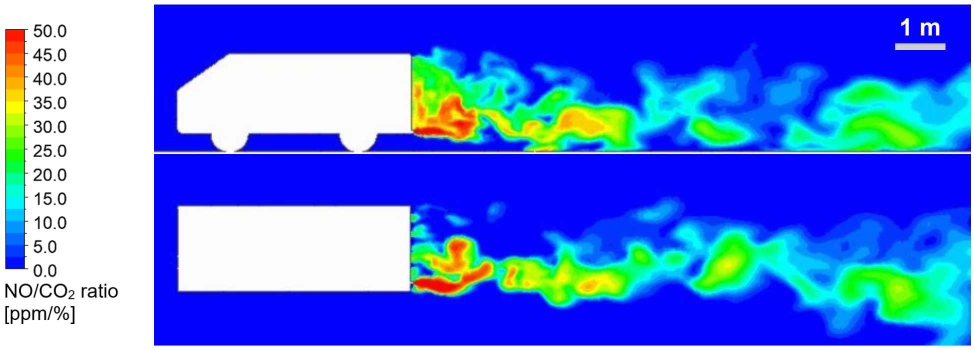


**Fig. 5.** Concentration ratio of $NO/CO_2$ under vehicle speed of 30 km/h, acceleration of 0 km/h/s and side wind of 0 m/s.

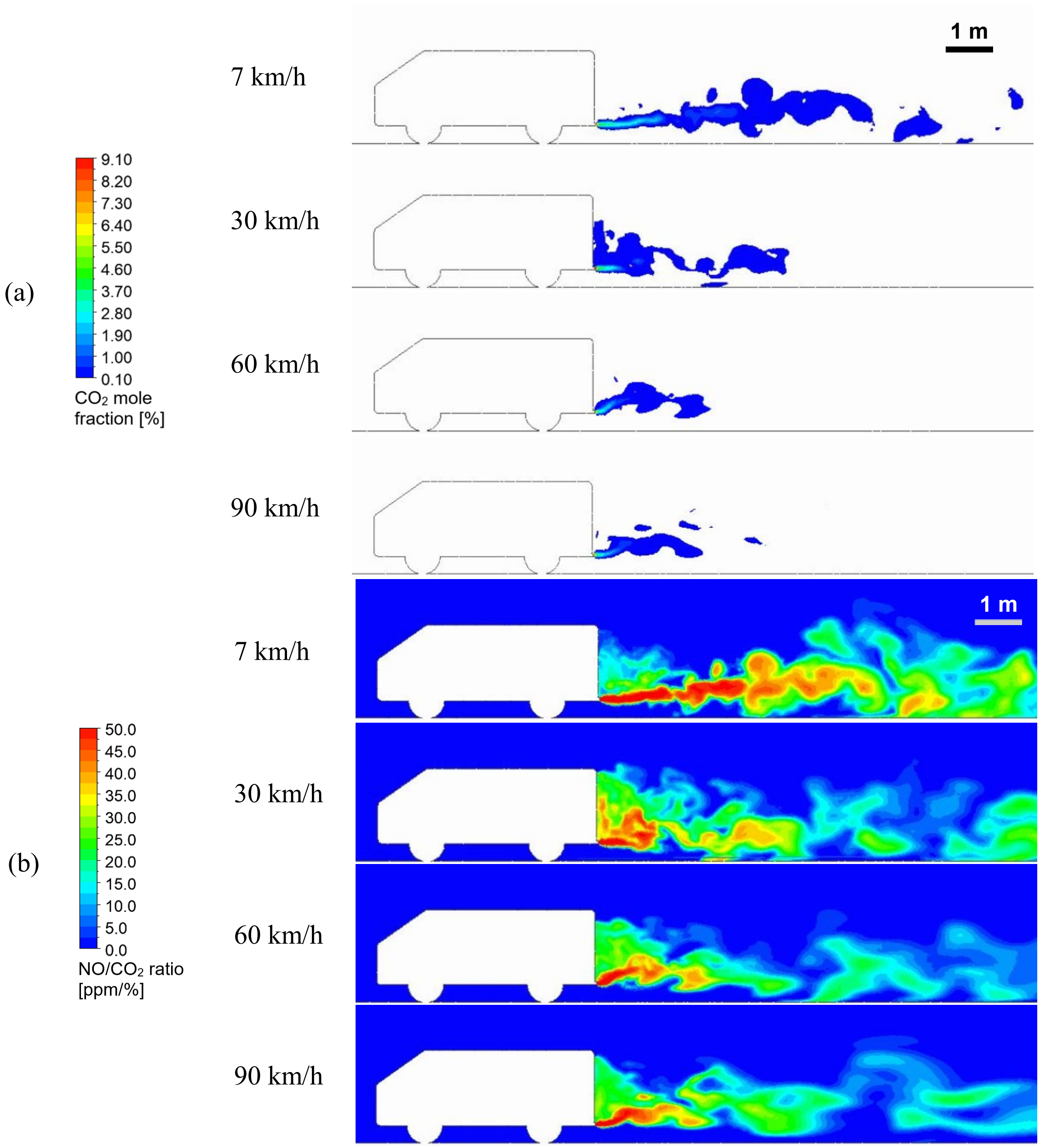


**Fig. 6.** Absolute volume concentrations of $CO_2$ (a) and concentration ratios of $NO/CO_2$ (b) under different vehicle speed conditions. Acceleration is 0 km/h/s and side wind is 0 m/s.

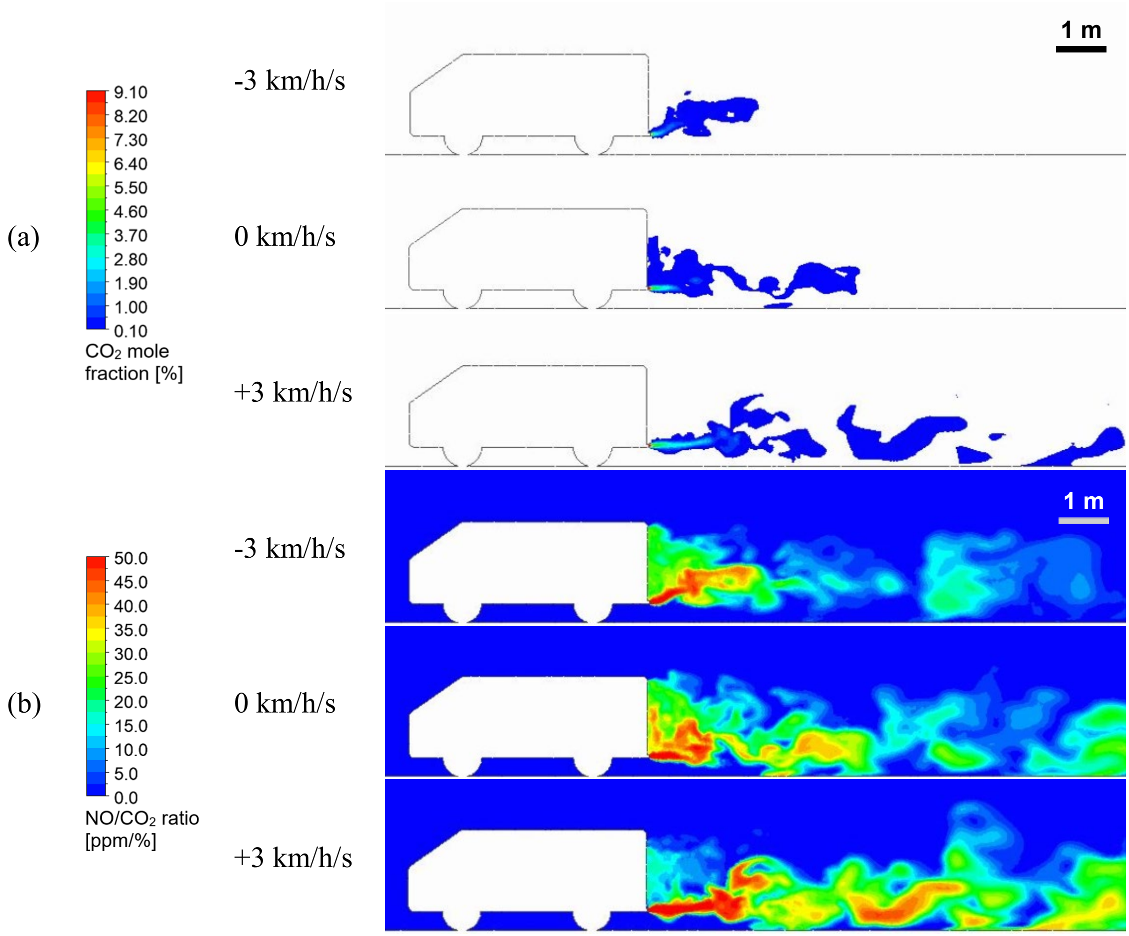


**Fig. 7.** Absolute volume concentrations of $CO_2$ (a) and concentration ratios of $NO/CO_2$ (b) under different acceleration conditions. Vehicle speed is 30 km/h and side wind is 0 m/s.

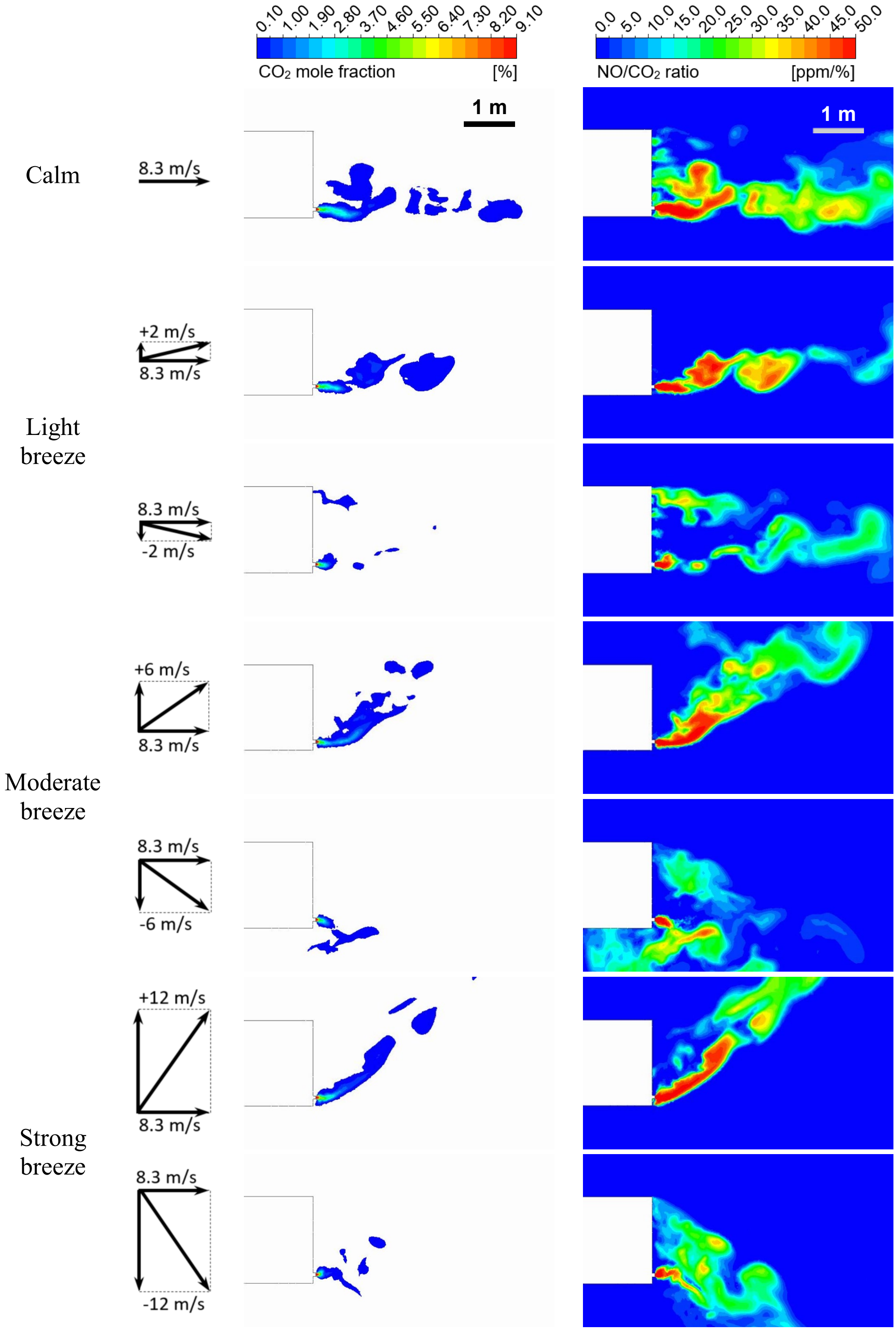


**Fig. 8.** Absolute volume concentrations of $CO_2$ and concentration ratios of $NO/CO_2$ under different side wind conditions. Vehicle speed is 30 km/h and accelerations is 0 km/h/s.